Journal of Materials Chemistry C

ROYAL SOCIETY OF CHEMISTRY

PAPER

View Article Online
View Journal | View Issue

Cite this: J. Mater. Chem. C, 2022, 10, 3418

Observation of dielectric dispersion and relaxation behavior in Ni^{2+}-substituted cobalt ferrite nanoparticles†

K. M. Srinivasamurthy,[a] A. El-Denglawey,*[b] K. Manjunatha,[c] Jagadeesha Angadi V.,*[d] M. C. Oliveira,[e] E. Longo,[e] S. R. Lázaro[f] and R. A. P. Ribeiro*[g]

Received 15th December 2021,
Accepted 21st January 2022

DOI: 10.1039/d1tc05980g

rsc.li/materials-c

In this study, a joint theoretical and experimental approach was employed to investigate the structural, electronic, magnetic and dielectric properties of novel ferrite (CNF) $Co_{1-x}Ni_xFe_2O_4$ (x = 0.0, 0.25, 0.5, 0.75 and 1.0) nanoparticles obtained using a low-cost combustion synthesis technique. Structural analysis indicated the single-phase formation of synthesized ferrite with a cubic spinel structure. Rietveld refinement was performed to estimate the lattice constant, strain and cationic distances. Vibrational Raman spectroscopy was employed to further confirm the monophasic cubic spinel structure with inverse cation distribution associated with the increase of the $T_{2g}(2)$ Raman mode, evidencing the presence of different cations at octahedral sites. The real part of the dielectric constant (ε') and the dielectric loss tangent ($\tan\delta$) were explored as a function of frequency, and the Nyquist complex impedance plots of all the samples were studied. The electrical properties of the samples at room temperature demonstrated the dispersion behavior associated with Maxwell–Wagner interfacial polarization mechanism and the hopping of charge carriers. DFT calculations complemented the experimental characterization, indicating a ferrimagnetic ground state for all models associated with band gap increases and dielectric constant reduction with an increasing amount of Ni. The low dielectric loss with Ni^{2+} substitution at higher frequencies makes CNF a promising candidate in the electronics industry for energy-harvesting devices.

1. Introduction

Spinel ferrites at the nano scale have received increasing attention in recent years due to their interesting features. For this reason, their advanced technological applications have included the fabrication of high-frequency devices, multi-chip inductors, and electromagnetic devices, and their use in spintronics, magnetic fluids, MRI, *etc.*[1–6] In the field of microwave instruments, because of their nonlinear phenomenological properties they have been applied as phase shifters, circulators and isolators.[7] For instance, the spinel ferrite AB_2O_4 (A = Co, Ni, Zn, Mn, Li and Mg; B = Fe) exhibits a cubic structure with the space group $Fd\bar{3}m$, where A is termed the tetrahedral site, B is denominated as the octahedral site, and oxygen atoms are located at the cubic close-packed arrangement. Cobalt ferrite has also drawn interest from the scientific community due to its remarkable magnetic, optical and electrical properties and potential technological applications. The most distinguishable feature of cobalt ferrite is the fine tuning of its physical properties, such as magnetic anisotropy, dielectric permittivity, resistivity and conductivity, through the substitution of other bivalent metal cations (M^{2+} = Ni, Zn, Mn, Mg, *etc.*) either at Co/Fe or at both lattice sites. These bivalent metal cations are promising candidates for current technological applications, including supercapacitor electrodes, permanent magnets, power transformer cores, sensing devices, adsorbents, catalysts, drug-delivery systems and magnetic probes among others.[8–13] The physical properties of $CoFe_2O_4$ are governed by the distribution of Co^{2+} and Fe^{3+} ions among tetrahedral (A) and octahedral (B) sites within the cubic spinel lattice. It is known that the substitution of

[a] Department of Physics, Bangalore University, 560056, Bangalore, India
[b] Department of Physics, College of University College at Turabah, Taif University, P.O. box 11099, Taif 21944, Saudi Arabia. E-mail: denglawey@yahoo.com
[c] Department of Physics, School of Engineering, Presidency University, 560064, Bangalore, India
[d] Department of Physics, P.C. Jabin Science College, Hubballi 580031, India. E-mail: jagadeeshbub@gmail.com
[e] CDMF-UFSCar, Federal University of São Carlos, 13565-905, São Carlos, SP, Brazil
[f] Department of Chemistry, State University of Ponta Grossa, 4748 General Carlos Cavalcanti Avenue, Ponta Grossa, PR, Brazil
[g] Department of Chemistry, Minas Gerais State University, 3001 Paraná Avenue, Divinópolis, MG, Brazil. E-mail: renan.ribeiro@uemg.br

† Electronic supplementary information (ESI) available. See DOI: 10.1039/d1tc05980g

bivalent M^{2+} at A- and B-sites alters the physical characteristics of ferrites markedly. Furthermore, the distribution of cations in the spinel depends on the synthesis method, type of substitution, sintering temperature, site at which the substituting cation is attaching, *etc.* The potentiality of changing the existing bivalent cation in the ferrite crystal structure is the key to driving the electrical and magnetic characteristics, and represents the fundamental basis for modern technology and science. A divalent metal cation M^{2+} in the crystal lattice alters the crystal edge by varying its A–O–B lengths, which in turn modify the superexchange interaction that governs the magnetic behavior of ferrites. This can be further extended to affect the dielectric properties by varying the bond lengths, and consequently the hopping of electrons between the cations.[14] The magnitudes of the modification of the dielectric properties depend on the substituting ion, its ionic radius, its preference site and electronic configuration. By choosing the proper divalent metal cation M^{2+} for the cobalt ferrite, the dielectric properties can be effectively tuned.

The conduction phenomenon and dielectric polarization in ferrites can be attributed to the hopping of charges between a divalent cation (M^{2+}) and Fe^{3+}.[15] When studying Mn^{2+}-substituted cobalt ferrite, Atif *et al.* concluded that the dielectric properties were strongly affected by both the distribution of cations mediated by Mn^{2+} doping and the change in morphology associated with the increase in Mn^{2+} content and its microstructure.[16] Kolekar *et al.* deliberated that the hopping of polarons is responsible for the conductivity in Mn^{2+}-substituted cobalt ferrite.[17] Tsay *et al.* reported that cobalt ferrite has a semiconducting nature and that the impedance and relaxation time of the grain boundaries are enhanced with increasing Ga content in Co–Mn ferrite, thus improving its electrical resistivity.[18] Yadav *et al.* reported that the grain size and cation redistribution are only responsible for the dielectric, electrical, magnetic, impedance and electrical modulus spectroscopic characteristics of synthesized $CoFe_2O_4$ spinel ferrite.[19] Thomas *et al.* studied Mg^{2+}-substituted cobalt ferrite nanoparticles and stated that the dielectric behavior could be explained by the Maxwell–Wagner interfacial polarization phenomenon.[20]

Despite the above considerations, cation distribution, dielectric relaxation and the polarization phenomenon are the admissible facts to correlate the dielectric dispersions of the spinel ferrite. Thus, the present work focused on the systematic study of the synthesis of Ni^{2+}-substituted cobalt ferrite $Co_{1-x}Ni_xFe_2O_4$ (x = 0.0, 0.25, 0.5, 0.75 and 1.0) nanoparticles *via* a combustion synthesis technique using mixture of fuels such as urea and glucose for the first time.[21] Rietveld refined XRD was performed to elucidate the cation–cation and cation–anion distances and bond angles. Cation substitution of the dopant was confirmed through Raman spectroscopy. The experimental results of the electrical and dielectric properties are discussed in detail using different existing models. In addition, theoretical calculations on the framework of density functional theory (DFT) were employed at the same Ni percentage in order to complement the discussion about the structural, electronic, dielectric and magnetic properties of the $Co_{1-x}Ni_xFe_2O_4$ material.

2. Experimental and computational details

2.1. Synthesis and characterization

Pure and Ni^{2+}-substituted $CoFe_2O_4$ nanoparticles were synthesized *via* a combustion synthesis technique. The detailed synthesis procedure and the grade of chemicals used are mentioned elsewhere.[22] Stoichiometric calculations to synthesize (CNF) $Co_{1-x}Ni_xFe_2O_4$ (x = 0.0, 0.25, 0.5, 0.75 and 1.0) nanoparticles are presented in the ESI.†

A schematic diagram of the solution combustion process for the CNF nanoparticles is shown in Fig. S1 (ESI†). The as-synthesized ferrite powder was finely ground using an agate mortar. The resulting fine powder was dissolved in 1% poly(vinyl alcohol) binder and compressed into pellets by applying a pressure of 5 ton sq cm^{-1} for 5 minutes and sintering at 800 °C for 2 hours in a furnace. The obtained samples were characterized using XRD. Rietveld refinement was performed for XRD data analysis using Fullprof Suite software. Raman spectra were collected using polarized argon laser radiation (λ = 514.5 nm) and recorded using a Renishaw inVia Reflex spectrometer coupled to an Edge filter. A Leica optical microscope with a 50× resolution objective lens was used to focus the incident light with a 2 μm diameter spot on the sample. All Raman spectra were corrected for the Bose–Einstein temperature factor. The parallel surfaces of the pellets were painted with silver paste to ensure good electrical contact. The impedance spectroscopy measurements were performed in the frequency range of 1 Hz to 20 MHz at room temperature using a Novocontrol Alfa A impedance analyzer.

2.2. Theoretical calculations

In this study, the CNF solid solution was investigated by means of density functional theory using the PBE0[23] hybrid functional implemented in the CRYSTAL17 package.[24] At room temperature, the end-members ($CoFe_2O_4$ and $NiFe_2O_4$) are found to have the inverse spinel structure ($Fd\bar{3}m$). As a first step, the experimental unit cell for both $CoFe_2O_4$ and $NiFe_2O_4$ oxides was minimized as a function of the total energy of the system. To investigate the magnetic properties, six magnetic models (FEM, AFM, FiM-I, FiM-II, FiM-III and FiM-IV) were used according to previous studies for normal and inverse spinel materials.[25] An overview of the resulting configurations can be found in the ESI.†

For such a proposal, the optimized primitive (14 atoms) unit cell was expanded to a conventional supercell (56 atoms), and the Co atoms were successively replaced by Ni to represent the x = 0.25, 0.50, and 0.75 stoichiometry following previous studies.[26] In all simulations the Co, and Ni were represented by all-electron 86-411d41G, and 8411d1 Gaussian basis sets were used to represent the O atoms.[27–29] The optimization process was truncated in 10^{-8} Hartree and five thresholds, with values set to 10^{-8}, 10^{-8}, 10^{-8}, 10^{-8} and 10^{-14} to control the level of accuracy of the Coulomb and exchange series. The irreducible Brillouin zone was represented for a sampling of k-points defined by a shrinking factor set to 8 × 8 (Gillat Web), in

accordance with the Monkhorst–Pack method.[30] The electronic structure for all compositions was investigated based on the density of states and band structure analysis using the optimized wavefunction.

3. Results and discussion

3.1 Structural analysis

The Rietveld refined X-ray diffractogram of the (CNF) $Co_{1-x}Ni_xFe_2O_4$ (x = 0.0, 0.25, 0.5, 0.75 and 1.0) nanoparticles is presented in Fig. 1.

The JCPDS file no. 22-1086 was used to index the following diffraction planes: (220), (311), (222), (400), (422), (511) and (440). The diffraction pattern confirms the formation of the spinel cubic structure with the space group $Fd\bar{3}m$. The lattice parameters of all samples were determined following previous experimental studies.[31] The estimated values lie between 8.3299 Å and 8.3064 Å, as listed in Table 1. The decreasing behavior can be attributed to the small ionic radius of Ni^{2+} (0.69 Å) in comparison with Co^{2+} (0.74 Å). The average ionic radii of tetrahedral (r_A) and octahedral sites (r_B) for each sample were estimated using the following equations:

$$r_A = \left(u - \frac{1}{4}\right)a\sqrt{3} - r_{O^{-2}}$$

$$r_B = \left(\frac{5}{8} - u\right)a - r_{O^{-2}}$$

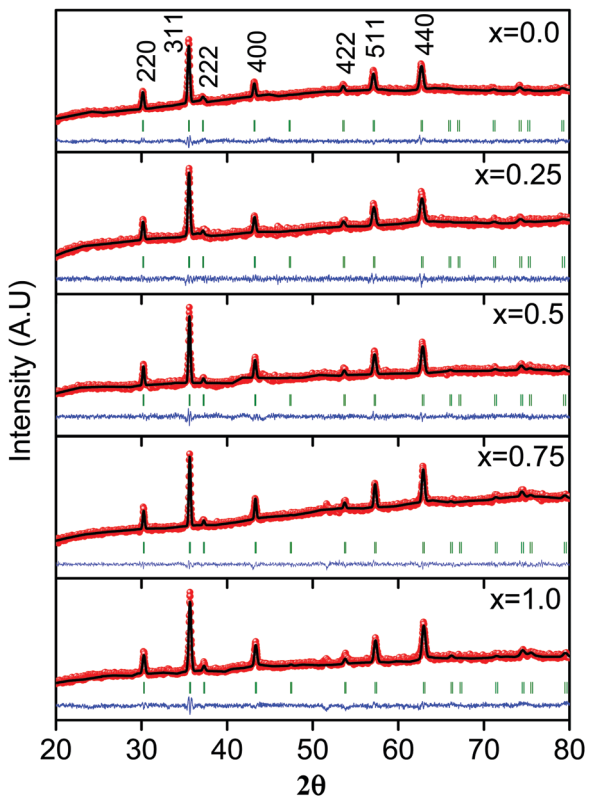

Fig. 1 Rietveld refined patterns of $Co_{1-x}Ni_xFe_2O_4$ ferrite nanoparticles.

Table 1 Estimated structural parameters and interionic distances between cation–cation (M–M), cation–anion (M–O) and bond angles for $Co_{1-x}Ni_xFe_2O_4$ (x = 0.0, 0.25, 0.5, 0.75 and 1.0) nanoparticles

	$Co_{1-x}Ni_xFe_2O_4$				
Parameters (Å)	x = 0.0	x = 0.25	x = 0.5	x = 0.75	x = 1.0
a	8.3299	8.3183	8.3137	8.3071	8.3064
Strain ($\times 10^{-4}$%)	35	37	33	32	37
r_A	0.5700	0.5674	0.5664	0.5649	0.5647
r_B	0.7125	0.7097	0.7085	0.7069	0.7067
d_A (d)	3.6069	3.6019	3.5999	3.5971	3.5967
d_B (b)	2.9451	2.9409	2.9393	2.9370	2.9367
d_{AO}	1.8900	1.8874	1.8863	1.8848	1.8847
d_{BO}	2.0337	2.0309	2.0297	2.0281	2.0279
d_{AE}	3.0864	3.0821	3.0804	3.0779	3.0777
d_{BE}	2.8037	2.7998	2.7982	2.7960	2.7958
d_{BEU}	2.9467	2.9426	2.9410	2.9387	2.9384
a_{th}	8.3297	8.3181	8.3135	8.3069	8.3062
M–M distances (Å)					
b	2.9451	2.9409	2.9393	2.9370	2.9367
c	3.4534	3.4486	3.4467	3.4439	3.4437
d	3.6069	3.6019	3.5999	3.5971	3.5967
e	5.4104	5.4029	5.3999	5.3956	5.3952
f	5.1010	5.0939	5.0911	5.0871	5.0866
M–O distances (Å)					
p	2.0325	2.0296	2.0285	2.0269	2.0267
q	1.8901	1.8874	1.8863	1.8848	1.8847
r	3.6191	3.6141	3.6121	3.6092	3.6089
s	3.6357	3.6307	3.6287	3.6258	3.6255
Bond angles (°)					
θ_1	123.34	123.35	123.35	123.34	123.35
θ_2	144.95	144.95	144.95	144.95	144.96
θ_3	92.85	92.86	92.85	92.86	92.86
θ_4	125.92	125.92	125.92	125.92	125.92
θ_5	74.48	74.48	74.48	74.48	74.45

where $r_{O^{-2}}$ is the radius of the oxygen ion (1.38 Å), u is the oxygen positional parameter (0.375 Å) and a is the lattice constant.

From the Rietveld refinement, the polyhedral structure of the $Co_{1-x}Ni_xFe_2O_4$ nanoparticles was elucidated and the interatomic distances the bond angles for and possible configurations are depicted in Fig. S2 (ESI†). The metal–metal cation distances, named as b, c, d, e and f, metal–oxygen distances, named as p, q, r, and s, along with the bond angles between the metal cations about the oxygen ion, named as θ_1, θ_2, θ_3, θ_4 and θ_5, were estimated from the equations listed in Table S3 (ESI†). The internal stain induced in the samples is due to the adjustment of the Ni^{2+}–O^{2-} bonds at the B-site and Fe^{3+}–O^{2-} at the A-site. The variation of internal strain values with Ni^{2+} substitution is because of the presence of the larger ionic radii of Fe^{3+} and Co^{2+} occupying both A- and B-sites.

It was observed that the decrease in the value of r_B is due to replacement of Co^{2+} by Ni^{2+}. The decrease in r_A can also be associated with the further migration of Fe^{3+} (0.67 Å) from an octahedral to a tetrahedral site with increasing Ni^{2+} content. The reduced size of the tetrahedral site can be assigned to the strong adjusting nature of Ni^{2+} at the octahedral site as a result of the inverse spinel structure distribution, without changing the symmetry of the cubic lattice along the [111] direction.

The theoretical lattice constant in terms of the average radii of tetrahedral and octahedral sites was determined using the

following equation:[32,33]

$$a_{th} = \frac{8}{3\sqrt{3}}\left[(r_A + r_{O^{-2}}) + \sqrt{3}(r_B + r_{O^{-2}})\right].$$

The interionic distances among A and B sites, *i.e.*, cation–anion distances at tetrahedral (d_{AO}) sites and octahedral (d_{BO}) sites, tetrahedral (d_{AE}), shared (d_{BE}) and unshared octahedral (d_{BEU}) edges, and the distance between the magnetic cations at tetrahedral (d_A) and octahedral (d_B) sites were determined using the following equations:

$$d_{AO} = a\sqrt{3}(u - 0.25)$$

$$d_{BO} = a\left(3u^2 - \frac{11u}{4} + \frac{43}{64}\right)^{1/2}$$

$$d_{AE} = a\sqrt{2}(2u - 0.5)$$

$$d_{BE} = a\sqrt{2}(1 - 2u)$$

$$d_{BEU} = a\left(4u^2 - 3u + \frac{11}{16}\right)^{1/2}$$

$$d_A = \frac{a}{4}\sqrt{3}$$

$$d_B = \frac{a}{4}\sqrt{2}$$

All the estimated parameters decrease as a function of Ni^{2+} substitution. This is attributed to the substitution being successful with the redistribution of cations among the A- and B-sites. A decrease in d_{AO} and d_{AE} is because of the shrinking of the A-site interstices with Ni^{2+} substitution, which preferentially occupy B-sites and replacing Fe^{3+} at the A-site. A-site interstices are very sensitive to small shifts in the anions, and the anions move inwards from their actual positions in the [111] direction resulting in a decrease in the A-site size relative to the ideal close packed arrangement of anions in a spinel cubic ferrite. There is no change in the tetrahedral symmetry of the interstices, which is governed by the respective bond angles of the spinel cubic lattice. A decrease in d_{BO} and d_{BE} is the result of the shifting of anions towards the octahedral interstices with Ni^{2+} substitution. Furthermore, a decrease in the size of B-site interstices results in the shortening of the shared edge d_{BE} and the unshared edge d_{BEU}. These observations indicate that the anions at the B-site are in close contact at these edges.

Therefore, the present system forms an inverse spinel structure, where Co/Ni^{2+} occupies the octahedral site and Fe^{3+} is located at both octahedral and tetrahedral sites. The distribution of cations among the tetrahedral and octahedral sites decides the structural, magnetic and electrical characteristics of the spinel ferrite.

For comparative purposes, the optimized lattice parameters and M–O bond distances for CNF models are summarized in Table S4 (ESI†), and show an excellent agreement with the experimental data (Table 1). In particular, the unit cell contraction was primarily associated with the local structural disorder that originated from Ni^{2+} substitution at octahedral [CoO_6] sites, but the intermetallic connection Fe_{tetra}–O–Co/Fe_{octa} in the inverse spinel structure induces a long-range distortion once both Fe–O and Co–O are affected by the Ni amount.

3.2 Raman spectra

A Raman spectral study is a powerful tool for investigating the lattice dynamics, vibrational spectra and the atomic structure of the nanoparticles.[34] Fig. 2 displays the Raman spectra of the CNF nanoparticles recorded in the region between 100 cm^{-1} and 800 cm^{-1} using laser excitation. Accurate peak locations of the obtained spectra were estimated by fitting the Lorentz peak shape function. Table 2 shows the wavenumbers associated with the Raman vibrational modes and polyhedral characteristics of the samples.

Group theory analysis predicts that ferrite nanoparticles show five Raman-active modes ($1A_{1g} + 1E_g + 3T_{2g}$).[35] The vibrational modes above 600 cm^{-1} are due to the tetrahedral site, whereas those below 600 cm^{-1} are assigned to the octahedral site. The A_{1g} mode is associated with the symmetric stretching of Fe–O bonds at the tetrahedral site and appears around 600–720 cm^{-1}. The E_g mode is related to the symmetric bending of O^{2-} with respect to Fe^{3+} at the octahedral site and appears around 250–350 cm^{-1}. The $T_{2g}(3)$ mode is due to the asymmetric bending vibration of O^{2-} with respect to Fe^{3+} and is located around 500–600 cm^{-1}. The $T_{2g}(2)$ mode is ascribed to the anti-symmetric stretching of O^{2-} and Fe^{3+} and appears around 450–500 cm^{-1}. Finally, the $T_{2g}(1)$ mode is due to the translational motion of Fe–O and is located around 180–220 cm^{-1}.[36]

In the present study, pure $CoFe_2O_4$ (CFO) forms a partially inverse spinel structure, whereas pure $NiFe_2O_4$ (NFO) crystallizes into a perfectly inverse spinel arrangement. Here, the tetrahedral A-sites are completely occupied by Fe^{3+} cations, while the remaining Fe^{3+} and Ni^{2+} are distributed over the octahedral B-sites. Our investigation involves the transition from CFO to NFO, with a step size of x = 0.25. The Raman vibrational frequency depends on the bond length and the reduced mass of the vibrating system. Lighter cations lead to higher wavenumber Raman lines, and *vice versa*. For pure CFO, only a fraction of Fe^{3+} occupies the tetrahedral site, and as the Ni^{2+} substitution increases the added Ni^{2+} are located at half the octahedral sites, whereas the Fe^{3+} cations are located at both octahedral and tetrahedral sites. Thus, a lighter cation occupying tetrahedral sites increases the Raman wavenumber corresponding to the A_{1g} mode. The wavenumber corresponding to the $T_{2g}(3)$ mode decreases with Ni^{2+} substitution, which can be explained by the fact that the substitution is restricted to octahedral sites. As for the $T_{2g}(2)$ mode, there is an increase in its wavenumber upon Ni^{2+} substitution. In addition, Fe^{3+} preferably replaces the fraction of Co^{2+} occupying the tetrahedral sites. The Raman modes of pure NFO show a doublet feature at E_g and $T_{2g}(1)$ due to local structures at the octahedral sites, which are occupied by either Ni^{2+} or Fe^{3+} ions.

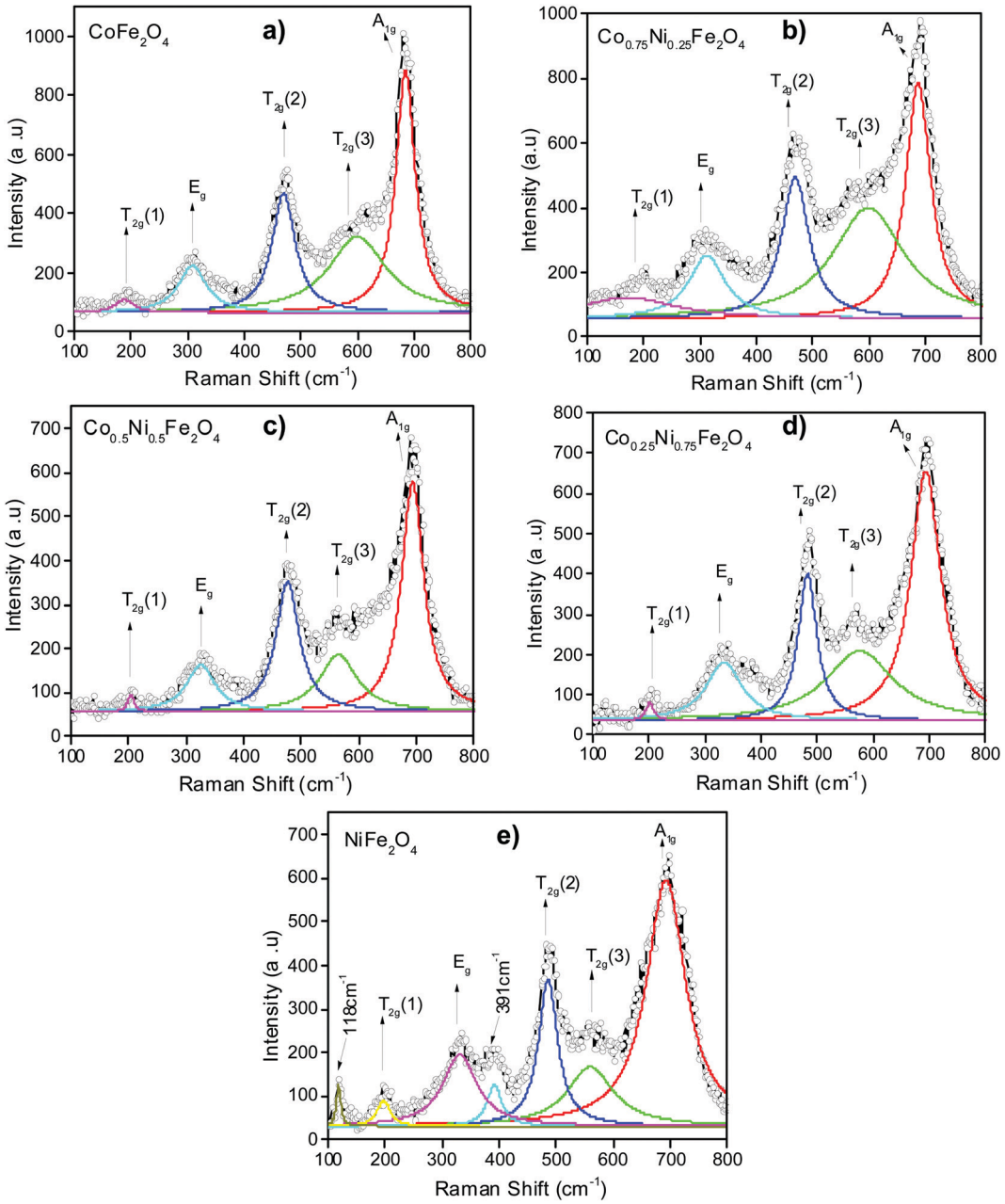

Fig. 2 Deconvoluted Raman spectra of CNF nanoparticles at room temperature, where a) x = 0.0, b) x = 0.25, c) x = 0.5, d) x = 0.75 and e) x = 1.0.

The peaks at 391 cm^{-1} and 119 cm^{-1} are from a unit cell comprising Fe and Ni ions at the octahedral site.[37]

Table 2 Vibrational data and assigned modes of $Co_{1-x}Ni_xFe_2O_4$ nanoparticles from room temperature Raman spectra

Peak no.	Observed peak (cm^{-1})					Raman-active mode	Assigned polyhedra
	x = 0.0	x = 0.25	x = 0.5	x = 0.75	x = 1.0		
1	684	685	693	693	692	A_{1g}	Tetrahedral
2	599	598	564	575	559	$T_{2g}(3)$	Octahedral
3	469	469	476	482	486	$T_{2g}(2)$	Octahedral
4	308	312	325	334	331	E_g	Octahedral
5	188	171	204	202	197	$T_{2g}(1)$	Octahedral

3.3 Dielectric analysis

Fig. 3a shows the frequency-dependent (1 Hz to 20 MHz) dielectric constant of the CNF nanoparticles at room temperature. The dielectric constant exhibits a high value at lower frequencies (1 Hz), decreasing sharply with increasing frequency (up to 100 Hz) and a steady state at higher frequencies up to 20 MHz. The high dielectric constant at low frequency is mostly ascribed to the interfacial space charge polarization impact due to the charge transporters amassed at the interface of conducting grains and non-conducting grain limits.[38–40] Moreover, the dielectric constant of the nanoparticles exhibits a Debye-type relaxation behavior, which diminishes at higher frequencies.

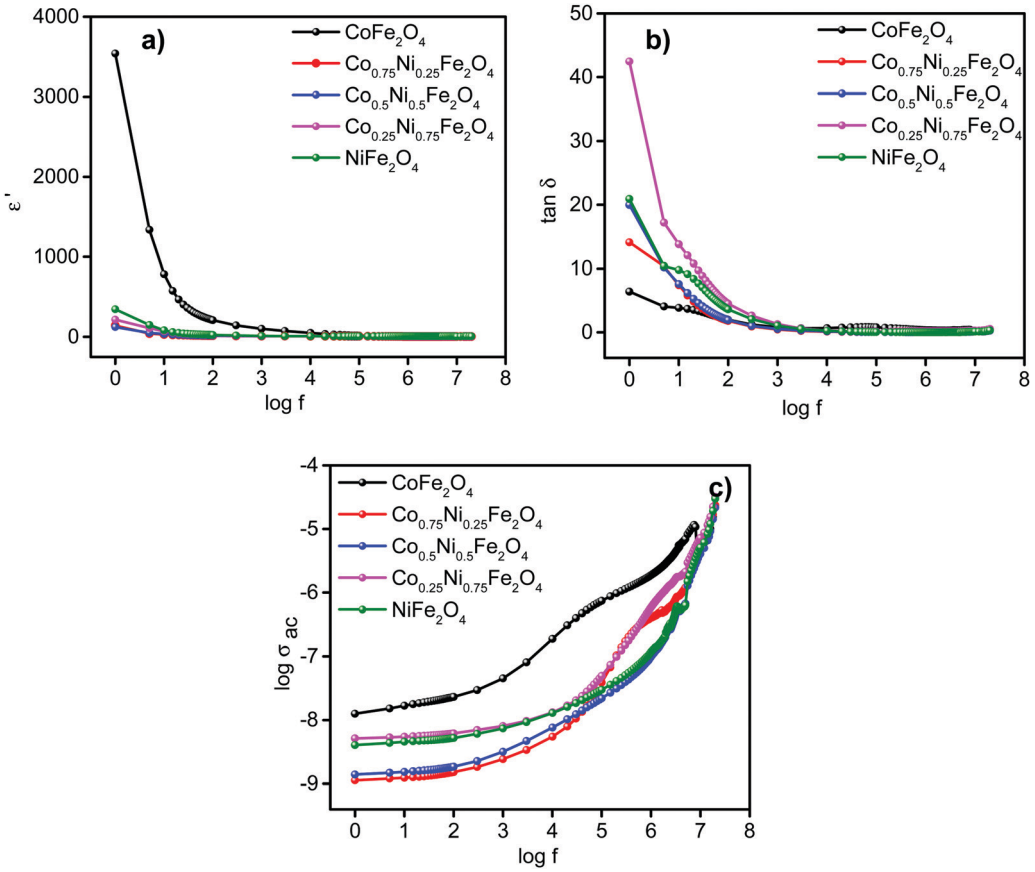

Fig. 3 Variation of (a) dielectric constant (ε'), (b) loss tangent (tan δ) and (c) ac conductivity (σ_{ac}) of $Co_{1-x}Ni_xFe_2O_4$ nanoparticles.

The dielectric loss tangent variation of the CNF nanoparticles as a function of frequency (1 Hz to 20 MHz) is shown in Fig. 3b. This variation is ascribed to the interfacial space charge polarization impact in the material.[41,42] It can be seen that the loss tangent increases with Ni^{2+} substitution. The dielectric loss value is marginally higher for samples with nickel substitution, which is probably due to the more modest grain size of the CNF nanoparticles. This more modest grain size arrangement may prompt a change in the conductivity of the material, which is further verified *via* an ac conductivity investigation. This result confirms that the dielectric constant and dielectric loss tangent can be significantly changed by substitution with nickel.

To comprehend the relaxation mechanism of ferrite nanoparticles, the ac conductivity (σ_{ac}) was determined from the relation $\sigma_{ac} = 2\pi f\varepsilon'\varepsilon_0 \tan\delta$, where f is the applied frequency, ε_0 is the absolute permittivity, ε' is the dielectric constant and tan δ is the dielectric loss of the material. The increase in ac conductivity for the samples may be due to the development of more modestly sized grains and grain boundary impacts arising from a large number of grain boundaries as a result of various polarization processes.[43] Furthermore, the conductivity in the samples is enhanced as the applied frequency is raised, which can be attributed to the hopping conveyance conductivity of the samples. It is known that the electrical conduction in a sample is a thermally enacted process and that the higher the conductivity of a material, the higher its dielectric constant. All electrical parameters of the CNF nanoparticles are summarized in Table S4 (ESI†).

Fig. 4 displays the frequency-dependent (1 Hz to 20MHz) real (Z') and imaginary (Z'') parts of the impedance of Ni^{2+}-substituted cobalt ferrite (CNF) nanoparticles. The Z' value decreases gradually as the applied frequency is increased and converges into one at higher frequencies. This behavior can be attributed to the loss of space charge polarization and the reduced grain boundary characteristics of the material.[44] This kind of trend is a clue regarding the enhancement of the material conduction and it is in good agreement with the obtained ac conductivity results previously mentioned.

The appearance of peaks in all samples confirms the existence of a relaxation phenomenon in the samples. The corresponding frequency f at which Z'' reaches its maximum is called the frequency of relaxation. It is then possible to estimate the relaxation time τ using the formula $\tau = 1/2\pi f$.[45,46] Peak widening and a shifting of Z'' maximum values to the higher frequency side clearly indicate that the electrical relaxation continues upon Ni^{2+} substitution. In addition, there is a decrease in the relaxation time in the samples with Ni^{2+} substitution. The estimated relaxation time τ for all samples is presented in Table 3.

A complex impedance investigation (plot of Z' *versus* Z'') recognizes the benefit of grain and grain boundary impacts of

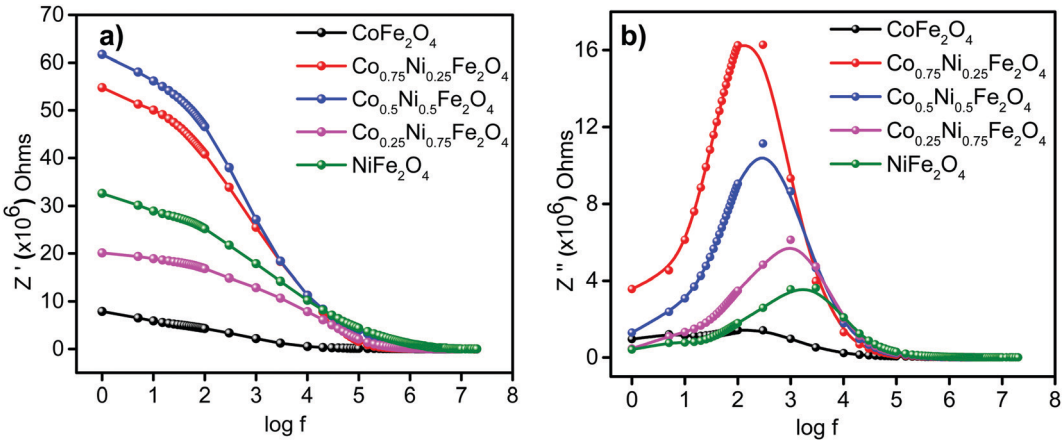

Fig. 4 Variation of (a) real (Z') and (b) imaginary (Z'') parts of the impedance of $Co_{1-x}Ni_xFe_2O_4$ nanoparticles as a function of the applied frequency.

the material. Cole–Cole or Nyquist plots of all CNF samples at room temperature are presented in Fig. 5.

From the plots in Fig. 5 it is possible to see a single semicircular arc whose center lies below the coordinate axes for all samples. This analysis explains that the contributory species for conductivity are either from a grain or grain boundary. The single semicircle clearly indicates the benefit of the grain boundary effect. The grain boundary in ferrite nanoparticles can be considered a parallel combination of resistance and capacitance, R_{gb} and C_{gb}, respectively. The grain boundary resistance (R_{gb}) is obtained from the diameter of the semicircles (R_{gb} = Z′, where Z'' = 0), while the grain boundary capacitance (C_{gb}) is estimated from the frequency (f_{gb}) at which the peak reaches its maximum, *i.e.*, $C_{gb} = 1/f_{gb}R_{gb}$. The relaxation time can be estimated as follows: $\tau_{gb} = 1/f_{gb} = R_{gb}C_{gb}$. The decrease in the radii of the semicircles with Ni^{2+} concentration indicates a decrease in the relaxation time.[47] The second peak that appears in the $x = 0.0$ composition is due to electrode polarization. As the Ni^{2+} concentration increases, the material impedance also increases, thus reducing the conductivity of the ferrites. The impedance reaches its maximum value for the x = 0.25 composition, which is a promising candidate for automotive applications.

Aiming to complement the experimental data about the electrical parameters of the CNF nanoparticles, DFT calculations were applied to obtain the static dielectric constant as a function of the Ni content. The calculation of the static dielectric constant tensor involves the sum of the electronic and ionic contributions. The electronic contribution of the dielectric constant (ε^{∞}) was obtained by applying an external static electric field to evaluate the perturbed electron density of the system (CPKS),[48–50] whereas the ionic contribution of the dielectric constant (ε_{vib}) was determined by calculating the vibrational frequencies.

For pure CFO, the dielectric constant was calculated as 7.836, while for the Ni-doped models the values were 7.680 (x = 0.25), 7.402 (x = 0.5), 7.120 (x = 0.75) and 7.106 (x = 1.0). The calculated values showed excellent agreement with previous theoretical and experimental data.[25,51,52] In particular, it was observed that the calculated dielectric constant was reduced as the Ni amount was increased. However, all values were calculated in the range of 7.1–7.9, indicating that all models exhibit good electrical properties for energy-harvesting applications.

Table 3 Impedance parameters of $Co_{1-x}Ni_xFe_2O_4$ nanoparticles from Cole–Cole plots

	Concentration (x)				
Parameter	0.0	0.25	0.5	0.75	1.0
R_{gb} (MΩ)	8	54	64	21	30
C_{gb} (pF)	1320	185	52	48	21
τ_{gb} (ms)	10.56	9.99	3.33	0.99	0.63

3.4 Magnetic and electronic structure analysis

In this section, DFT calculations were analyzed to explain the magnetic and electronic structure of the CNF nanoparticles. As previously mentioned, six magnetic models (FEM, AFM, FiM-I, FiM-II, FiM-III and FiM-IV) were considered for all compositions, and the relative energy values are summarized in Table 4. In all cases, the FiM-I configuration corresponds to the magnetic ground state, which is described as the Néel-ferrimagnetic model, where magnetic cations at tetrahedral sites are ordered in parallel with their first neighbors, while an antiparallel spin ordering with octahedral sites describes the next-neighboring exchange coupling[53] Moreover, it was observed that AFM and other ferromagnetic models (II, III and IV) showed a similar energy difference to FiM-I, indicating that the magnetic phase transition can exhibit both ferrimagnetic to antiferromagnetic orientation and spin reorganization, consequently creating other ferrimagnetic orientations. Similar results were calculated for $CoFe_2O_4$ and $NiFe_2O_4$ with the PW1PW exchange–correlation functional, confirming that the PBE0 results are in accordance with experimental and theoretical predictions.[25,52,53]

Another important aspect about CNF nanoparticles is their electronic structural analysis. Herein, the band structure and atom-resolved density of states profiles were considered, as presented in Fig. 6. Separated plots for band structure are included in Fig. S3 (ESI†) depicting in detail the spin-up and spin-down channels. As described in previous studies, investigation of the band gap energy and the localization of atomic states near the

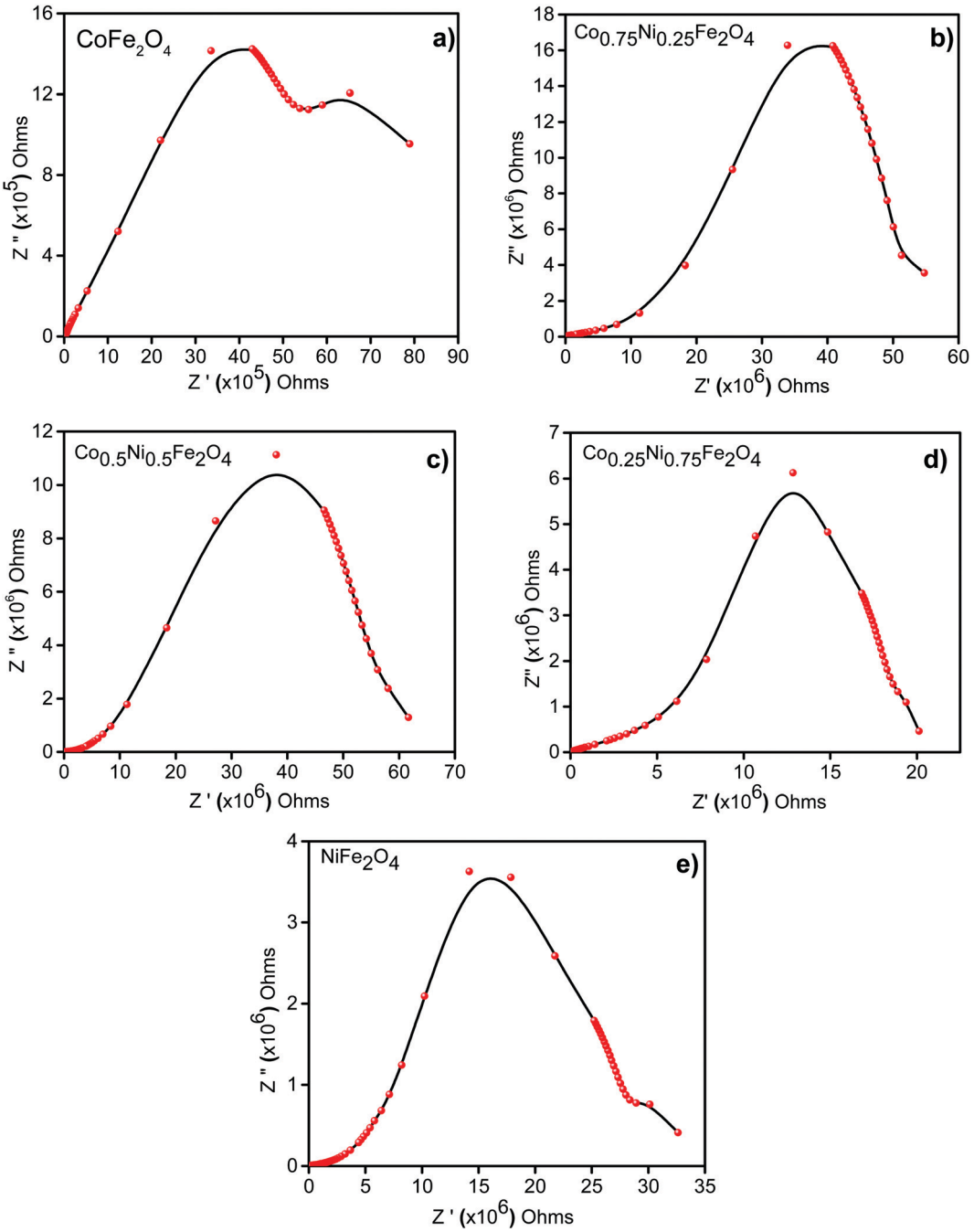

Fig. 5 Cole–Cole or Nyquist plots of $Co_{1-x}Ni_xFe_2O_4$ nanoparticles, where a) x = 0.0, b) x = 0.25, c) x = 0.5, d) x = 0.75 and e) x = 1.0.

Fermi level can help us to understand the charge-storage properties of ferrites [57].

Table 4 Relative energy (meV f.u.$^{-1}$) computed at the DFT/PBE0 level for different magnetic configurations of $Co_{1-x}Ni_xFe_2O_4$ models

	FEM	AFM	FiM-I	FiM-II	FiM-III	FiM-IV
$CoFe_2O_4$	666.67	315.61	0.00	372.88	219.47	285.60
$Co_{0.75}Ni_{0.25}Fe_2O_4$	501.37	282.02	0.00	313.49	321.20	282.29
$Co_{0.5}Ni_{0.5}Fe_2O_4$	504.01	314.73	0.00	397.39	238.57	285.51
$Co_{0.25}Ni_{0.75}Fe_2O_4$	522.48	273.33	0.00	141.86	211.20	276.74
$NiFe_2O_4$	501.85	268.80	0.00	359.14	186.86	274.65

It can be first observed that the flat-like band for the conduction band minimum (CBM) induces similar values for direct and indirect band gap values. With increasing Ni amounts, the valence band maximum (CBM) moves from the *M* to the *Γ* point, indicating a redistribution of electron density associated with the M–O (M = Co, Ni) bonding path. In addition, the bands become more degenerate near the Fermi level, which could help the structure to store charges, thus increasing the specific capacitance.

With regard to the band gap values, $CoFe_2O_4$ exhibits an indirect (*M*–*Γ*) excitation around 3.17 eV, and with increasing

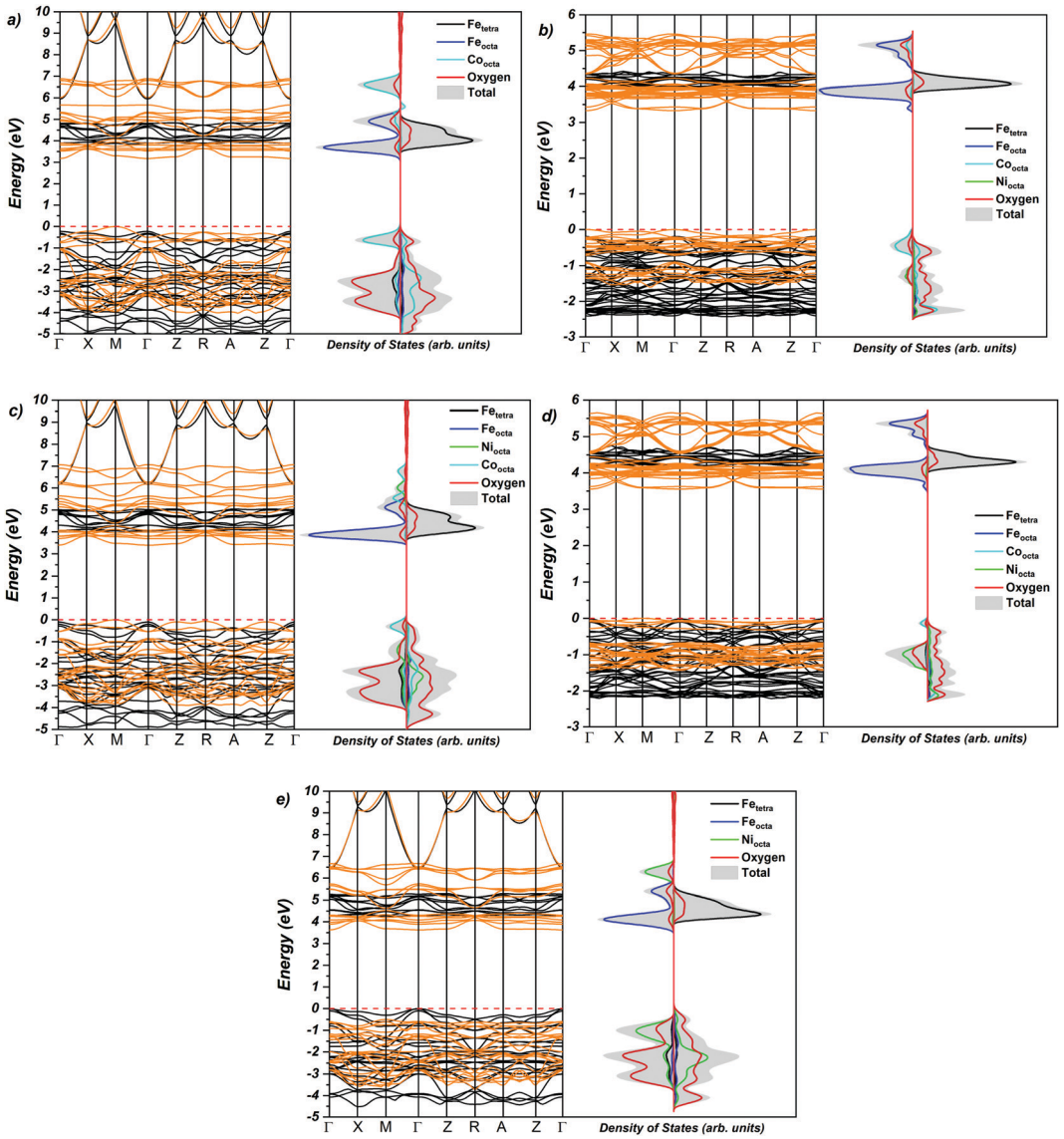

Fig. 6 Band structure and atom-resolved density of states profiles for $Co_{1-x}Ni_xFe_2O_4$ models, where (a) x = 0.0, (b) x = 0.25, (c) x = 0.5, (d) x = 0.75 and (e) x = 1.0.

Ni amounts the band gap becomes higher (3.33 for x = 0.25, Γ–M/Γ–Γ/Γ–Z; 3.39 for x = 0.5, M–Γ; 3.56 for x = 0.75, Γ–M/M–M; and 4.28 eV for x = 1.0 Γ–Γ). This can be associated with the Ni ($3d^8$) configuration, which exhibits a $t_{2g}^6e_g^2$ occupation, in comparison with that of Co ($3d^7$), which exhibits a $t_{2g}^5e_g^2$ spin distribution. Ulpe and co-workers investigated in depth the electronic structure of several spinel materials, confirming that the band gap description is challenging for DFT calculations.[52] Herein, the calculated values at PBE0 allowed us to relate the increased band gap value to the variation in the Ni amount, which is in agreement with previous experimental data.[54,55]

Another important aspect to consider about the electronic structure of CNF nanoparticles is the atomic state localization along the valence/conduction bands. In all cases, the valence band is mainly composed of O (2p) states of [BO_6] clusters, while the conduction band is formed by a mixed composition of both empty levels of Fe centers at tetrahedral and octahedral sites. Therefore, the electronic excitation or electron hopping mechanism can be associated with the electron density redistribution along the [Co/NiO_6]–[FeO_4/FeO_6] bonding path, resulting in a redox process since Ni/Co-centers are oxidized and Fe-centers are reduced. This helps to describe the nature of electron excitation, charge distribution and storage along the chemical structure of mixed spinel ferrites.

4. Conclusions

Pure and Ni^{2+}-substituted cobalt ferrite (CNF) nanoparticles were synthesized *via* a low-cost combustion synthesis route. XRD patterns confirmed the phase purity of the samples. Structural analysis indicated the fingerprints associated with

the inverse spinel structure in terms of the atomic positions, lattice parameters and bonding factors. Room-temperature Raman studies illustrated the standard vibration modes occurring at the tetrahedral and octahedral sites of the spinel ferrite. A dielectric study probed the dielectric constant, loss tangent and ac conductivity affected by Ni^{2+} substitution in the cobalt ferrite nanoparticles. Impedance showed that a significant variation in the material resistance was due to the grain boundary contribution mediated by the Ni^{2+} content in the nanoparticles, thus altering the cation distribution and the microstructure. A complex impedance investigation explored the existence of an electrical relaxation mechanism as a result of the polarization phenomenon and the hopping mechanism. High impedance and low dielectric loss with Ni^{2+} substitution were observed. DFT calculations were used to complement the experimental analysis and provide an atomic-level description of the dielectric constant increase, variation in band gap values and magnetic ground-state orientation. Based on such analyses, CNF nanoparticles can be described as promising candidates to be applied in the electronics industry for the fabrication of energy-harvesting devices.

Conflicts of interest

There are no conflicts to declare.

Acknowledgements

A. El-Denglawey express sincere thank to Taif University Researchers Supporting Project Number (TURSP-2020/45) Taif University, Taif, Saudi Arabia. Furthermore, his research work was partially supported by the Ministry of Education and Science of the Russian Federation (project no. 3.5346.2017/8.9). The State University of Ponta Grossa, the Minas Gerais State University (UEMG), CAPES, CNPq, FAPEMIG, and the Fundação Araucária (Brazil) funded the theoretical component of this work. M. C. Oliveira gratefully thanks the financial assistance from FAPESP (project no. 2021/01651-1). E. Longo acknowledges the financial support from FAPESP (project no. 2013/07296-2). R. A. P. Ribeiro is grateful for the financial assistance from FAPEMIG (project no. APQ-00079-21) and UEMG for the Productivity Program. The authors thank the Federal University of Rio de Janeiro's (COPPE-UFRJ) National Laboratory for Scientific Computing (LNCC) and High-Performance Computing Center (NACAD) for providing computational resources for the Lobo Carneiro supercomputer. The authors would also like to thank the National Center for High-Performance Computing (CENAPAD) at UNICAMP and UFMG for providing computing resources.

References

1 M. Ansari, A. Bigham and H. A. Ahangar, *Mater. Sci. Eng., C*, 2019, **105**, 110084.
2 M. Radmansouri, E. Bahmani, E. Sarikhani, K. Rahmani, F. Sharifianjazi and M. Irani, *Int. J. Biol. Macromol.*, 2018, **116**, 378–384.
3 B. Abraime, K. El Maalam, L. Fkhar, A. Mahmoud, F. Boschini, M. Ait Tamerd, A. Benyoussef, M. Hamedoun, E. K. Hlil, M. Ait Ali, A. El Kenz and O. Mounkachi, *J. Magn. Magn. Mater.*, 2020, **500**, 166416.
4 M. Z. Ahsan, F. A. Khan and M. A. Islam, *J. Electron. Mater.*, 2019, **48**, 7721–7729.
5 P. Monisha, P. Priyadharshini, S. S. Gomathi and K. Pushpanathan, *J. Phys. Chem. Solids*, 2021, **148**, 109654.
6 M. Shaterian, A. Aghaei, M. Koohi, M. Teymouri and A. Mohammadi-Ganjgah, *Polyhedron*, 2020, **182**, 114479.
7 A. V. Humbe, J. S. Kounsalye, M. V. Shisode and K. M. Jadhav, *Ceramics International*, 2018, **44**, 5466–5472.
8 O. Karaagac, B. B. Yildiz and H. Köçkar, *J. Magn. Magn. Mater.*, 2019, **473**, 262–267.
9 R. Jabbar, S. H. Sabeeh and A. M. Hameed, *J. Magn. Magn. Mater.*, 2020, **494**, 165726.
10 T. P. Niesen and M. R. De Guire, *Solid State Ionics*, 2002, **151**, 61–68.
11 M. Yoshimura, W. L. Suchanek and K. Byrappa, *MRS Bull.*, 2011, **25**, 17–25.
12 W. H. V. Aulock, *J. Appl. Phys.*, 1966, **37**, 939–946.
13 V. S. Kumbhar, A. D. Jagadale, N. M. Shinde and C. D. Lokhande, *Appl. Surf. Sci.*, 2012, **259**, 39–43.
14 M. Atif, T. Rafique, A. U. Rehman, H. Wahab, W. Khalid, Z. Ali and M. Nadeem, *J. Mater. Sci.: Mater. Electron.*, 2020, **31**, 10970–10980.
15 S. Akhter, D. P. Paul, M. A. Hakim, D. K. Saha, H. N. Das, A. Parveen and B. Anjuman, *Mater. Res.*, 2018, **21**(4), e20170655.
16 M. Atif, M. Idrees, M. Nadeem, M. Siddique and M. W. Ashraf, *RSC Adv.*, 2016, **6**, 20876–20885.
17 S. M. Ansari, R. D. Bhor, K. R. Pai, S. Mazumder, D. Sen, Y. D. Kolekar and C. V. Ramana, *ACS Biomater. Sci. Eng.*, 2016, **2**, 2139–2152.
18 C.-Y. Tsay, Y.-H. Lin, Y.-M. Wang, H.-Y. Chang, C.-M. Lei and S.-U. Jen, *AIP Adv.*, 2016, **6**, 055909.
19 R. S. Yadav, I. Kuřitka, J. Vilcakova, J. Havlica, J. Masilko, L. Kalina, J. Tkacz, J. Švec, V. Enev and M. Hajdúchová, *Adv. Nat. Sci.: Nanosci. Nanotechnol.*, 2017, **8**, 045002.
20 N. Thomas, P. V. Jithin, V. D. Sudheesh and V. Sebastian, *Ceram. Int.*, 2017, **43**, 7305–7310.
21 K. M. Srinivasamurthy, V. J. Angadi, S. P. Kubrin, S. Matteppanavar, D. A. Sarychev and B. Rudraswamy, *J. Supercond. Novel Magnet.*, 2019, **32**, 693–704.
22 K. M. Srinivasamurthy, J. Angadi V, S. P. Kubrin, S. Matteppanavar, D. A. Sarychev, P. M. Kumar, H. W. Azale and B. Rudraswamy, *Ceram. Int.*, 2018, **44**, 9194–9203.
23 C. Adamo and V. Barone, *J. Chem. Phys.*, 1999, **110**, 6158–6170.
24 R. Dovesi, A. Erba, R. Orlando, C. M. Zicovich-Wilson, B. Civalleri, L. Maschio, M. Rérat, S. Casassa, J. Baima, S. Salustro and B. Kirtman, *Wiley Interdiscip. Rev.: Comput. Mol. Sci.*, 2018, **8**, e1360.

25 A. C. Ulpe, K. C. L. Bauerfeind and T. Bredow, *ACS Omega*, 2019, **4**, 4138–4146.
26 G. Pilania, V. Kocevski, J. A. Valdez, C. R. Kreller and B. P. Uberuaga, *Commun. Mater.*, 2020, **1**, 84.
27 M. D. Towler, N. L. Allan, N. M. Harrison, V. R. Saunders, W. C. Mackrodt and E. Aprà, *Physical Review B*, 1994, **50**, 5041–5054.
28 R. Dovesi, F. Freyria Fava, C. Roetti and V. R. Saunders, *Faraday Discuss.*, 1997, **106**, 173–187.
29 T. Bredow, K. Jug and R. A. Evarestov, *Phys. Status Solidi B*, 2006, **243**, R10–R12.
30 H. J. Monkhorst and J. D. Pack, *Phys. Rev. B*, 1976, **13**, 5188–5192.
31 P. Bera, R. V. Lakshmi, B. H. Prakash, K. Tiwari, A. Shukla, A. K. Kundu, K. Biswas and H. C. Barshilia, *Phys. Chem. Chem. Phys.*, 2020, **22**, 20087–20106.
32 in *Magnetic Ceramics*, ed. R. Valenzuela, Cambridge University Press, Cambridge, 1994, pp. i–vi.
33 B. D. Cullity, *Elements of X-ray Diffraction*, Addison-Wesley Publishing Company, 1978.
34 A. Kumar, J. Shen, W. Yang, H. Zhao, P. Sharma, D. Varshney and Q. Li, *J. Supercond. Novel Magnet.*, 2018, **31**, 1173–1182.
35 K. Praveena, H.-W. Chen, H.-L. Liu, K. Sadhana and S. R. Murthy, *J. Magn. Magn. Mater.*, 2016, **420**, 129–142.
36 G. V. M. Jacintho, A. G. Brolo, P. Corio, P. A. Z. Suarez and J. C. Rubim, *The J. Phys. Chem. C*, 2009, **113**, 7684–7691.
37 C. O. Ehi-Eromosele, B. I. Ita, E. E. Iweala, S. A. Adalikwu and P. A. L. Anawe, *Bull. Mater. Sci.*, 2015, **38**, 1465–1472.
38 K. S. Cole and R. H. Cole, *J. Chem. Phys.*, 1941, **9**, 341–351.
39 H.-z. Duan, F.-l. Zhou, X. Cheng, G.-h. Chen and Q.-l. Li, *J. Magn. Magn. Mater.*, 2017, **424**, 467–471.
40 K. Ali, J. Iqbal, T. Jan, I. Ahmad, D. Wan and I. Ahmad, *Mater. Chem. Phys.*, 2017, **195**, 283–294.
41 A. Ditta, M. A. Khan, M. Junaid, R. M. A. Khalil and M. F. Warsi, *Phys. B: Condens. Matter*, 2017, **507**, 27–34.
42 M. Ajmal, M. U. Islam, G. A. Ashraf, M. A. Nazir and M. I. Ghouri, *Phys. B: Condens. Matter*, 2017, **526**, 149–154.
43 K. S. Hemalatha, G. Sriprakash, M. V. N. A. Prasad, R. Damle and K. Rukmani, *J. Appl. Phys.*, 2015, **118**, 154103.
44 S. Vangchangyia, E. Swatsitang, P. Thongbai, S. Pinitsoontorn, T. Yamwong, S. Maensiri, V. Amornkitbamrung and P. Chindaprasirt, *J. Am. Ceram. Soc.*, 2012, **95**, 1497–1500.
45 K. P. Padmasree, D. K. Kanchan and A. R. Kulkarni, *Solid State Ionics*, 2006, **177**, 475–482.
46 T. Badapanda, S. Sarangi, S. Parida, B. Behera, B. Ojha and S. Anwar, *J. Mater. Sci.: Mater. Electron.*, 2015, **26**, 3069–3082.
47 A. A. Kadam, S. S. Shinde, S. P. Yadav, P. S. Patil and K. Y. Rajpure, *J. Magn. Magn. Mater.*, 2013, **329**, 59–64.
48 M. Ferrero, M. Rérat, B. Kirtman and R. Dovesi, *J. Chem. Phys.*, 2008, **129**, 244110.
49 M. Ferrero, M. Rérat, R. Orlando and R. Dovesi, *J. Comput. Chem.*, 2008, **29**, 1450–1459.
50 M. Ferrero, M. Rérat, R. Orlando and R. Dovesi, *J. Chem. Phys.*, 2008, **128**, 014110.
51 P. Chand, S. Vaish and P. Kumar, *Phys. B: Condens. Matter*, 2017, **524**, 53–63.
52 A. C. Ulpe, K. C. L. Bauerfeind, L. I. Granone, A. Arimi, L. Megatif, R. Dillert, S. Warfsmann, D. H. Taffa, M. Wark, D. W. Bahnemann and T. Bredow, *Z. Phys. Chem.*, 2020, **234**, 719–776.
53 G. A. Sawatzky, F. Van Der Woude and A. H. Morrish, *Phys. Rev.*, 1969, **187**, 747–757.
54 K. Dileep, B. Loukya, N. Pachauri, A. Gupta and R. Datta, *J. Appl. Phys.*, 2014, **116**, 103505.
55 B. S. Holinsworth, D. Mazumdar, H. Sims, Q.-C. Sun, M. K. Yurtisigi, S. K. Sarker, A. Gupta, W. H. Butler and J. L. Musfeldt, *Appl. Phys. Lett.*, 2013, **103**, 082406.

